# DASPy: A Python Toolbox for DAS Seismology

**Minzhe Hu[1] and Zefeng Li[1, 2*]**


1. *Laboratory of Seismology and Physics of Earth's Interior, School of Earth and*

   *Space Sciences, University of Science and Technology of China, Hefei, China*

2. *Mengcheng National Geophysical Observatory, University of Science and*

   *Technology of China, Mengcheng, China*


Corresponding author: Zefeng Li (zefengli@ustc.edu.cn)

**Abstract**

Distributed acoustic sensing (DAS) has emerged as a novel technology in geophysics, owing to its high sensing density, cost-effectiveness, and adaptability to extreme environments. Nonetheless, DAS differs from traditional seismic acquisition technologies in many aspects: big data volume, equidistant sensing, measurement of axial strain (strain rate), and noise characteristics. These differences make DAS data processing challenging for new hands. To lower the bar of DAS data processing, we develop an open-source Python toolbox called DASPy which encompasses classic seismic data processing techniques, including preprocessing, filter, spectrum analysis, and visualization, and specialized algorithms for DAS applications, including denoising, waveform decomposition, channel attribute analysis, and strain-velocity conversion. Using openly available DAS data as examples, this paper makes an overview and tutorial on the eight modules in DASPy to illustrate the algorithms and practical applications. We anticipate DASPy to provide convenience for researchers unfamiliar with DAS data and help facilitate the rapid growth of DAS seismology.

**1 Introduction**

Distributed acoustic sensing (DAS) is an emerging vibration monitoring technology increasingly utilized in geophysics. It converts fiber optic cables into an ultradense seismic array with meter-scale spacing and a frequency range of 0.01 Hz to 100 kHz. DAS recovers axial strain or strain rate along the fiber-optic cable by measuring the subtle optical phase shift of backscattered light within the fiber (Lindsey & Martin, 2021; Zhan, 2019). Over recent years, it has been demonstrated useful in many seismological applications such as earthquake monitoring (Z. Li et al., 2021; Z. Li & Zhan, 2018; Nayak et al., 2021; Zeng et al., 2022), source properties (Chen, 2023; J. Li, Kim, et al., 2023; J. Li, Zhu, et al., 2023), microseisms (Sladen et al., 2019; Williams et al., 2019, 2022; Xiao et al., 2022), subsurface imaging (Cheng et al., 2021; Luo et al., 2021; Nayak & Ajo-Franklin, 2021; Yang, Atterholt, et al., 2022), and fault zone structures (Atterholt, Zhan, & Yang, 2022; Jousset et al., 2018; Lindsey et al., 2019; Yang, Zhan, et al., 2022). It has also been applied in volcanology (Jousset et al., 2022; Nishimura et al., 2021), glaciology (Hudson et al., 2021; Walter et al., 2020), marine biology (Bouffaut et al., 2022; Landrø et al., 2022; Rørstadbotnen et al., 2023; Wilcock et al., 2023), and traffic monitoring (Lindsey, Yuan, et al., 2020; X. Wang et al., 2021).

DAS is distinct from conventional seismometers in several key aspects, including the voluminous data, the image-like nature, the regular spacing of sensors, and the uniaxial measurement (Z. Li, 2021). The noise composition of DAS tends to be more complex

52    due to its different self-noise, common-mode noise, and traffic noise for often along-

53    road fibers (Bakku, 2015; Costa et al., 2019; Lindsey, Rademacher, et al., 2020; Zhirnov

54    et al., 2019). These differences often require different processing techniques from those

55    for conventional seismometers, making it challenging for researchers newly using DAS

56    data. Inspired by the success of ObsPy for conventional seismic data processing

57    (Beyreuther et al., 2010), we believe that a new processing package specifically

58    designed for DAS data could facilitate the development of DAS seismology.

59

60    In this paper, we design an open-source Python package named DASPy for DAS data

61    processing. This package comprises two primary components: a set of basic tools

62    including modules for preprocessing, filtering, frequency attributes and visualization,

63    and another set of advanced tools including modules for channel analysis, waveform

64    decomposition, denoising and strain-velocity conversion (Fig. 1). As follows, we

65    showcase the key functionalities using various publicly available datasets (Fig. 2) and

66    ensure that the experiments can be easily replicated by readers.

67

68    **2 Basic Tools**

69    *2.1 Classic processing techniques*

70    Typical seismic data processing includes filtering, frequency attribute analysis and

71    certain preprocessing methods. We wrap these techniques for 2D DAS data, eliminating

72    the need for iterating over channels. For example, the Python code below bandpass

73    filters the data from the RAPID dataset (Wilcock & Ocean Observatories Initiative.,

74    2023; http://piweb.ooirsn.uw.edu/das/; Figure 2a) between 15 and 27 Hz and yields a

75    spectrogram averaged over 100 channels and a frequency-wavenumber (FK) spectrum

76    (Figure 3). This dataset was collected offshore central Oregon and recorded various

77    signals including fin whale calls, northeast Pacific blue whale A and B calls, and ship

78    noises (Wilcock et al., 2023).

79

```
>>> from daspy.basic_tools.filter import bandpass
>>> from daspy.basic_tools.freqattributes import spectrogram, fk_transform
>>>
>>> data_filtered = bandpass(data, fs, 15, 27, detrend=True, taper=0.04)
>>> spec, f1, t = spectrogram(data[4880-50:4880+50], fs=fs, nperseg=256, noverlap=246,
                              nfft=1024, detrend=True)
>>> fk, f2, k = fk_transform(data, dx, fs)
```

80

81

82    *2.2 Visualization*

83    The function, `plot`, can be used to visualize 2D DAS data. It offers a number of

84    optional parameters to accommodate the users' requirements for plotting a variety of

85    data types, such as waveforms, spectra, spectrograms, and FK spectra. Below is the

86    Python code for visualizing the data in the previous example: unfiltered and filtered

87    data, the spectrogram and the FK spectrum (Figure 3). The bandpass filtered waveform

88    reveals high-frequency fin whale calls, with amplitudes approximately four to five

89    orders of magnitude lower than the ocean wave signals (Figure 3b). The spectrogram

90    demonstrates the sequential production of high- and low-frequency calls by the fin

91    whale (Figure 3c). The FK spectrum reveals an apparent velocity of this acoustic signal

92    exceeding 1400 m/s along the axial direction of the optical cable (Figure 3d).

93

```
>>> from daspy.basic_tools.visualization import plot
>>>
>>> fig, ax = plt.subplots(4, 1, figsize=(7,8))
>>> plot(data, dx=dx, fs=fs, ax=ax[0], transpose=True, x0=xmin*dx, xaxis=False)
>>> plot(data_filtered, dx=dx, fs=fs, ax=ax[1], transpose=True, x0=xmin*dx, axis=False)
>>> plot(Zxx, fs=fs, obj='spectrogram', ax=ax[2], f=f1, t=t, vmin=2e-8, vmax=3e-6,
        ylim=[0, 40])
>>> plot(fk, obj='fk', ax=ax[3], f=f2, k=k, xlim=[-0.025, 0.025], ylim=[0, 40],
        vmin=0.05, vmax=0.2)
>>> plt.tight_layout(pad=0.5)
```

94

95

96    **3 Advanced Tools**

97    *3.1 Channel analysis*

98    DAS channels have equidistant spacing but the location of each channel is often

99    unknown and requires tap tests. Besides, the linearity and ground coupling of the fibers

100   often need to be taken care of. We develop three functions for channel location and

101   quality analysis: channel location interpolation, turning point detection, and low-quality

102   channel checking.

103

104   Channel location interpolation for DAS is calculated using two types of inputs: points

105   with known channel numbers, and optional fiber spatial track points without channel

106   numbers. Points with known channel numbers are typically acquired through tap tests

107   and are often sparse. The spatial fiber track points are used to constrain the array

108   geometry. They are optional but dense track points are particularly useful for accurate

109 location interpolation. Fig. 2a shows examples of the two DAS arrays of the RAPID

110 dataset (Wilcock & Ocean Observatories Initiative., 2023). In DASPy, we implemented

111 the interpolation method used by the RAPID team, in which interpolation is performed

112 after the coordinates are projected to the Universal Transverse Mercator (UTM)

113 coordinate system.

114

115 The turning point detection function determines the points where the fiber strike varies

116 noticeably based on the given channel coordinates or based on waveform coherency

117 across neighboring channels. The application of the coordinate-based detection

118 function to Brady's geothermal field DAS array (University of Wisconsin, 2016a;

119 https://gdr.openei.org/submissions/829; Fig. 2c) produces results consistent with those

120 of Piana Agostinetti et al. (2022). As across-channel waveform coherency is not only

121 affected by the fiber strike angle, but also controlled by other factors including the

122 quality of the backscattered light, coupling conditions and small-scale scatterers at

123 different locations, its results could be less stable than those of coordinate-based

124 computations assuming the coordinates are accurate. However, when the coordinates

125 are unavailable or inaccurate, inference from across-channel waveform coherency

126 could be a suitable alternative.

127

128 The channel quality checking function detects segments with obvious poor coupling

129 (e.g., zip-tied loops of telecommunication cables) by identifying outliers of waveform

130  energy along the fiber. It fits the waveform energy (the square of the amplitudes)

131  variations with channels by a high-order polynomial and removes the fitted polynomial

132  from the data. A threshold of four times of standard deviation below the median is set

133  to identify the outliers. We assume that poor coupling tends to be spatially continuous.

134  Hence, isolated normal values among a group of outliers would be identified as bad

135  channels and vice versa. Using this function, we assess the channel quality of

136  Ridgecrest DAS (Fig. 2d) with 15 seconds of traffic noise (Atterholt, 2021;

137  https://data.caltech.edu/records/1955, Fig. 4). Our waveform-based detection results

138  are generally consistent with the hand-picked results of Atterholt, Zhan, Shen, et al.

139  (2022) (Fig. 4b-f), except for the initial segment which was identified from a priori

140  knowledge during field installation. It is noteworthy that the spikes (Fig. 4a) do not

141  significantly influence the low-quality channel detection because we use a robust fit for

142  the waveform energy (abnormal points are excluded from fitting).

143

144  *3.2 Data denoising*

145  As aforementioned, DAS data are often mixed with complex types of noise. DASPy

146  integrates functions for the removal of typical noise types, including spike noise (Bakku,

147  2015), common-mode noise (Lindsey, Rademacher, et al., 2020), stochastic noise

148  (Costa et al., 2019), and coherent noise. DASPy constructs a denoising module that

149  incorporates three methods that take advantage of different noise properties.

150

151    Spikes are unusually large amplitudes (Fig. 5a) and could be caused by laser frequency

152    drift or laser noise (Zhirnov et al., 2019). The spike removal function first applies the

153    across-channel median filter and then the across-time median filter to generate a median

154    map from the absolute amplitudes. Points with amplitudes exceeding a predefined

155    threshold of the median map are identified as spikes. All spikes are subsequently

156    substituted with interpolated values from adjacent channels. The spike removal function

157    is validated using an earthquake waveform recorded by the Stanford-1 DAS array (Fig.

158    2b and Fig. 5a-b; Biondi et al., 2017; Martin et al., 2017).

159

160    Common-mode noise, also known as in-phase noise is generated by vibrations of the

161    optoelectronic system and arises on all channels simultaneously (Fig. 5d). DASPy

162    employs spatial averaging of waveforms to obtain common mode noise. Subsequently,

163    we compute the correlation coefficient with the channel record and the common-mode

164    noise, multiply the common-mode noise by the coefficient, and subtract it from the

165    channel record. We evaluate the common-mode noise removal algorithm using a

166    segment of offshore channels of the RAPID dataset (Wilcock & Ocean Observatories

167    Initiative, 2023; Fig. 2a). The processing effectively mitigates the common-mode noise

168    (Fig. 5d-e).

169

170    The inherent stochastic noise in DAS data is primarily caused by instrumental

171    deficiencies such as sampling error and phase noise (Costa et al., 2019). The fast

172    discrete curvelet transform (FDCT) (E. Candès et al., 2006; E. J. Candès & Donoho,

173    2004) is used to obtain an effective non-adaptive sparse representation of the image-

174    like DAS seismic data and remove stochastic noise (Atterholt, Zhan, Shen, et al., 2022).

175    The basis functions of curvelet transform are defined as polar wedges in the FK domain

176    and represent the object position, scale, and angle. The curvelet denoising function uses

177    a silent DAS recording to estimate stochastic noise. After FDCT, the amplitude of the

178    curvelet coefficients is used as an empirical threshold. By default, DASPy employs a

179    soft threshold to remove stochastic noise in the curvelet domain. We apply curvelet

180    denoising to the spike-removed waveform of Stanford-1 DAS (Biondi et al., 2017;

181    Martin et al., 2017; Fig. 2b and Fig. 5b), resulting in a notable reduction in stochastic

182    noise before the arrival of P waves (Fig. 5c).

183

184    Coherent noise can be defined as any coherent signal that are not of interest. For

185    example, for studies on an earthquake, a traffic signal is coherent noise; for studies on

186    traffic footprints, an earthquake signal is coherent noise. Coherent noise can be

187    removed by applying velocity screening in either the curvelet transform or the FK

188    transform. In this case, coherent noise removal is treated as wavefield decomposition

189    based on apparent velocity, which will be elaborated upon in the subsequent section.

190

191    *3.3 Wavefield decomposition*

192    Image processing techniques, such as the 2D Fast Fourier Transform (e.g., FK

193    transform in DAS data processing) and FDCT, have been widely used in the

194    decomposition of 2D DAS wavefields, such as the separation of seismic signals and

195    traffic noise and the separation of direct seismic waves and locally scattered seismic

196    waves (Atterholt, Zhan, Shen, et al., 2022; Williams et al., 2022). DASPy integrates the

197    FK filtering and curvelet windowing techniques in the decomposition module. Note

198    that FK filtering often causes various artifacts, particularly edge artifacts caused by

199    discontinuities at the waveform's edge, and star-like artifacts originating from

200    discontinuities in the FK domain. To minimize these artifacts, DASPy employs cosine

201    tapers (e.g. Tukey window) on the waveforms, as well as the filtering window in the

202    FK domain.

203

204    Both wavefield decomposition techniques are evaluated on stripping traffic noise from

205    seismic waveform from the Ridgecrest DAS array (Z. Li et al., 2021; Fig. 2d). The

206    results show that both techniques effectively enhance the signal-to-noise ratio (Fig. 6).

207    For those traffic noises with particularly large amplitudes, the FK filtering achieves

208    more thorough separation but creates some star-like artifacts. Conversely, curvelet

209    windowing appears to leave more large-amplitude parts of traffic signals, but with

210    fewer artifacts.

211

212    *3.4 Conversion to ground motions*

213 DAS measures strain or strain rate, in contrast to ground-motion velocity and

214 displacement used in typical seismology studies. Strain rate can be converted to particle

215 velocity by multiplying apparent phase velocity. The difficulty of such conversion lies

216 in the accurate estimation of apparent phase velocity of every wiggle. DASPy integrates

217 three methodologies for converting strain/strain rate into ground-motion velocity: FK

218 rescaling (Lindsey, Rademacher, et al., 2020), curvelet transform (Yang, Atterholt, et

219 al., 2022), and time-domain slowness determination (Lior et al., 2021). The FK

220 rescaling method is implemented by multiplying each point in the FK domain by its

221 corresponding apparent velocity (slop in the FK domain). Similarly, the basis functions

222 of the curvelet transform, which are defined in the FK domain, also correspond to

223 varying velocity ranges. The curvelet transform conversion method multiplies each

224 curvelet coefficient by the median velocity of its basis function. The coefficients of the

225 largest scale basis functions, which represents waves with all velocity ($-\infty$ to $+\infty$), is

226 set to zero. The time-domain slowness determination method obtains the apparent

227 velocity at each time step by searching for the maximal semblance.

228

229 These three methods are tested using an $M_L$ 4.3 earthquake recorded by a co-located

230 DAS and seismometer array in the Brady Hot Springs (University of Wisconsin, 2016b;

231 University of Wisconsin, 2016c; https://gdr.openei.org/submissions/848;

232 https://gdr.openei.org/submissions/846; Fig. 3c), following H. F. Wang et al. (2018). We

233 define a nodal geophone and a DAS channel whose distance is less than 5 m as a

234   geophone-channel pair. Among 238 geophones and 8,621 DAS channels, we match a

235   total of 344 geophone-channel pairs. For each geophone-channel pair, we find the

236   corresponding linear DAS segment (Fig. 2c) and rotate the three-component geophone

237   recording to the axial fiber direction. The original DAS strain rate recordings are

238   integrated to strain in the time domain, and converted to velocity using FK rescaling,

239   curvelet transform and time-domain slowness determination methods respectively (Fig.

240   7). We correct the DAS data timing (-1.048 s) using the GPS timing of nodal

241   seismometers, and cross-correlate the waveforms of each geophone-channel pair with

242   time shift less than ±0.01 seconds. All waveforms are bandpass filtered to 1-5 Hz.

243

244   We evaluate the cross-correlation coefficient between the converted DAS velocity and

245   the rotated geophone velocity. For all 344 geophone-channel pairs, 104, 68 and 0 pairs

246   obtain cross-correlation coefficients greater than 0.7 after FK rescaling, curvelet

247   transformation and time-domain slowness determination, respectively. For this

248   particular case, the curvelet transform and the time-domain slowness determination

249   have limitations. Most linear segments consist of about 100 channels, which is not quite

250   enough for curvelet transform at larger scales. The largest scale curvelet coefficients,

251   which are set to zero, miss more details, resulting in smaller amplitudes of the converted

252   waveforms (Fig. 7). As for time-domain slowness determination methods, the

253   assumption of monochromatic wavefields makes it difficult to recover the complex

254   shallow surface scattered waves and earthquake coda waves.

255

**4 Discussion and conclusions**

257    DASPy aims to offer a user-friendly, integrated Python toolkit that facilitates the

258    analysis and processing of DAS data. Overall, the toolkit includes "basic tools" of

259    preprocessing, filtering, spectrum analysis, and visualization techniques and "advanced

260    tools" of channel attribute analysis, noise removal, wavefield decomposition, and

261    strain-velocity conversion.

262

263    DASPy operates in the form of functions, which are designed to accommodate as many

264    optional parameters as possible, and with sensible default values. All functions within

265    DASPy are implemented as methods of the "daspy.DASdata" class. This approach is

266    advantageous in that data attributes are stored within the class and avoid the need for

267    manual entry. Below is the Python code for reading DAS data into "daspy.Section",

268    calling its method to bandpass filter the data between 1 and 5 Hz, convert to velocity

269    by FK rescaling and to show the final waveform.

```
>>> from daspy import read
>>>
>>> sec = read('test.h5')
>>> sec.bandpass(1, 5).fk_rescaling()
>>> sec.plot()
```

270

271    Calling functions and using methods of "daspy.Section" class are functionally

272    equivalent, providing flexibility to suit users' needs.

273

274 DASPy is currently programmed in pure Python for ease of use and modification but

275 in some cases computational efficiency is compromised. Consequently, processing

276 continuous data with a large number of channels and/or a high sampling rate could take

277 a long time. As an example, downsampling a 30-second waveform recorded at 1000 Hz

278 by a 10,000-channel DAS array takes 12.08 seconds. Therefore, we suggest that users

279 consider implementing CPU parallelization when undertaking large tasks. Future

280 development of DASPy could include exploring the potential of shared libraries to

281 replace computationally intensive functions.

282

283 Finally, we welcome users to contribute to the improvement and expansion of the

284 DASPy project by developing new functions and/or modules (such as earthquake

285 monitoring, ambient noise imaging, and traffic detection algorithms) upon the

286 foundation of existing functionalities. Users are recommended to fork the DASPy

287 repository on Github (https://github.com/HMZ-03/DASPy/) and submit their

288 modifications and additions through pull requests.

289

290 **Data and Resources**

291 The RAPID dataset is openly available at http://piweb.ooirsn.uw.edu/das/. The traffic

292 signals recorded by the Ridgecrest DAS can be downloaded from

293 https://data.caltech.edu/records/31emd-wmv98. The Stanford DAS-1 dataset from

294 PubDAS is accessible via the link https://app.globus.org/file-

295 manager?origin_id=706e304c-5def-11ec-9b5c-f9dfb1abb183&origin_path=%2F. The

296 earthquake waveforms recorded by Brady's Geothermal Field DAS and seismometer

297 array are available at https://gdr.openei.org/submissions/848 and

298 https://gdr.openei.org/submissions/846. The DASPy python package is open source

299 and available at https://github.com/HMZ-03/DASPy/. All websites were last accessed

300 in March 2024.

301

305

306 **Declaration of Competing Interests**

307 The authors acknowledge there are no conflicts of interest recorded.

308

309  **References**

310  Atterholt, J. (2021). Earthquake Waveforms from Curvelet-denoising Paper (Data

311      Supplement) (1.0) [Data set]. CaltechDATA. https://doi.org/10.22002/D1.1955

312  Atterholt, J., Zhan, Z., Shen, Z., & Li, Z. (2022). A unified wavefield-partitioning

313      approach for distributed acoustic sensing. *Geophysical Journal International*,

314      *228*(2), 1410–1418. https://doi.org/10.1093/gji/ggab407

315  Atterholt, J., Zhan, Z., & Yang, Y. (2022). Fault zone imaging with distributed

316      acoustic sensing: body-to-surface wave scattering. *Journal of Geophysical*

317      *Research: Solid Earth*, *127*(6), 1–17. https://doi.org/10.1029/2022jb024329

318  Bakku, S. K. (2015). Fracture Characterization from Seismic Measurements in a

319      Borehole. *PhD Thesis*.

320  Beyreuther, M., Barsch, R., Krischer, L., Megies, T., Behr, Y., & Wassermann, J.

321      (2010). ObsPy: A python toolbox for seismology. *Seismological Research*

322      *Letters*, *81*(3), 530–533. https://doi.org/10.1785/gssrl.81.3.530

323  Biondi, B., Martin, E., Cole, S., Karrenbach, M., & Lindsey, N. (2017). Earthquakes

324      analysis using data recorded by the Stanford DAS array. In *SEG Technical*

325      *Program Expanded Abstracts 2017* (pp. 2752–2756).

326      https://doi.org/10.1190/segam2017-17745041.1

327  Bouffaut, L., Taweesintananon, K., Kriesell, H. J., Rørstadbotnen, R. A., Potter, J. R.,

328      Landrø, M., et al. (2022). Eavesdropping at the Speed of Light: Distributed

329    Acoustic Sensing of Baleen Whales in the Arctic. *Frontiers in Marine Science*,

330    *9*(July), 1–13. https://doi.org/10.3389/fmars.2022.901348

331  Brady's Geothermal Field DAS and DTS Surface and Borehole Array Metadata [Data

332    set]. (2016). University of Wisconsin. https://doi.org/10.15121/1261907

333  Brady's Geothermal Field DAS Earthquake Data [Data set]. (2016). University of

334    Wisconsin. https://doi.org/10.15121/1334285

335  Brady's Geothermal Field Nodal Seismometer Earthquake Data [Data set]. (2016).

336    University of Wisconsin. https://doi.org/10.15121/1334284

337  Candès, E., Demanet, L., Donoho, D., & Ying, L. (2006). Fast discrete curvelet

338    transforms. *Multiscale Modeling and Simulation*, *5*(3), 861–899.

339    https://doi.org/10.1137/05064182X

340  Candès, E. J., & Donoho, D. L. (2004). New tight frames of curvelets and optimal

341    representations of objects with piecewise C2 singularities. *Communications on*

342    *Pure and Applied Mathematics*, *57*(2), 0219–0266.

343    https://doi.org/10.1002/cpa.10116

344  Chen, X. (2023). Source parameter analysis using distributed acoustic sensing – an

345    example with the PoroTomo array. *Geophysical Journal International*, 2207–

346    2213.

347  Cheng, F., Chi, B., Lindsey, N. J., Dawe, T. C., & Ajo-Franklin, J. B. (2021).

348    Utilizing distributed acoustic sensing and ocean bottom fiber optic cables for

349    submarine structural characterization. *Scientific Reports*, *11*(1), 1–14.

350    https://doi.org/10.1038/s41598-021-84845-y

351 Costa, L., Martins, H. F., Martín-López, S., Fernández-Ruiz, M. R., & González-

352    Herráez, M. (2019). Fully Distributed Optical Fiber Strain Sensor With 10−12

353    ε/√Hz Sensitivity. *Journal of Lightwave Technology*, *37*(18), 4487–4495.

354    https://doi.org/10.1109/JLT.2019.2904560

355 Hudson, T. S., Baird, A. F., Kendall, J. M., Kufner, S. K., Brisbourne, A. M., Smith,

356    A. M., et al. (2021). Distributed Acoustic Sensing (DAS) for Natural

357    Microseismicity Studies: A Case Study From Antarctica. *Journal of Geophysical*

358    *Research: Solid Earth*, *126*(7), 1–19. https://doi.org/10.1029/2020JB021493

359 Jousset, P., Currenti, G., Schwarz, B., Chalari, A., Tilmann, F., Reinsch, T., et al.

360    (2018). Dynamic strain determination using fibre-optic cables allows imaging of

361    seismological and structural features. *Nature Communications*, *13*(1).

362    https://doi.org/10.1038/s41467-022-29184-w

363 Jousset, P., Currenti, G., Schwarz, B., Chalari, A., Tilmann, F., Zuccarello, L., et al.

364    (2022). Fibre optic distributed acoustic sensing of volcanic events. *Nature*

365    *Communications*. https://doi.org/10.1038/s41467-022-29184-w

366 Landrø, M., Bouffaut, L., Kriesell, H. J., Potter, J. R., Rørstadbotnen, R. A.,

367    Taweesintananon, K., et al. (2022). Sensing whales, storms, ships and

368    earthquakes using an Arctic fibre optic cable. *Scientific Reports*, *12*(1), 1–10.

369    https://doi.org/10.1038/s41598-022-23606-x

370    Li, J., Zhu, W., Biondi, E., & Zhan, Z. (2023). Earthquake focal mechanisms with

371        distributed acoustic sensing. *Nature Communications*, *14*(1), 4181.

372        https://doi.org/10.1038/s41467-023-39639-3

373    Li, J., Kim, T., Lapusta, N., Biondi, E., & Zhan, Z. (2023). The break of earthquake

374        asperities imaged by distributed acoustic sensing. *Nature*, *620*(October 2022).

375        https://doi.org/10.1038/s41586-023-06227-w

376    Li, Z. (2021). Recent advances in earthquake monitoring i: Ongoing revolution of

377        seismic instrumentation. *Earthquake Science*, *34*(2), 177–188.

378        https://doi.org/10.29382/eqs-2021-0011

379    Li, Z., & Zhan, Z. (2018). Pushing the limit of earthquake detection with distributed

380        acoustic sensing and template matching: A case study at the Brady geothermal

381        field. *Geophysical Journal International*, *215*(3), 1583–1593.

382        https://doi.org/10.1093/gji/ggy359

383    Li, Z., Shen, Z., Yang, Y., Williams, E., Wang, X., & Zhan, Z. (2021). Rapid

384        Response to the 2019 Ridgecrest Earthquake With Distributed Acoustic Sensing.

385        *AGU Advances*, *2*(2). https://doi.org/10.1029/2021av000395

386    Lindsey, N. J., & Martin, E. R. (2021). Fiber-Optic Seismology. *Annual Review of*

387        *Earth and Planetary Sciences*, 309–338.

388    Lindsey, N. J., Craig Dawe, T., & Ajo-Franklin, J. B. (2019). Illuminating seafloor

389        faults and ocean dynamics with dark fiber distributed acoustic sensing. *Science*,

390        *366*(6469), 1103–1107. https://doi.org/10.1126/science.aay5881

391     Lindsey, N. J., Yuan, S., Lellouch, A., Gualtieri, L., Lecocq, T., & Biondi, B. (2020).

392         City-Scale Dark Fiber DAS Measurements of Infrastructure Use During the

393         COVID-19 Pandemic. *Geophysical Research Letters*, *47*(16), 1–8.

394         https://doi.org/10.1029/2020GL089931

395     Lindsey, N. J., Rademacher, H., & Ajo-Franklin, J. B. (2020). On the Broadband

396         Instrument Response of Fiber-Optic DAS Arrays. *Journal of Geophysical*

397         *Research: Solid Earth*, *125*(2), 1–16. https://doi.org/10.1029/2019JB018145

398     Lior, I., Sladen, A., Mercerat, D., Ampuero, J. P., Rivet, D., & Sambolian, S. (2021).

399         Strain to ground motion conversion of distributed acoustic sensing data for

400         earthquake magnitude and stress drop determination. *Solid Earth*, *12*(6), 1421–

401         1442. https://doi.org/10.5194/se-12-1421-2021

402     Luo, B., Trainor-Guitton, W., Bozdag, E., LaFlame, L., Cole, S., & Karrenbach, M.

403         (2021). Horizontally orthogonal distributed acoustic sensing array for

404         earthquake- And ambient-noise-based multichannel analysis of surface waves.

405         *Geophysical Journal International*, *222*(3), 2147–2161.

406         https://doi.org/10.1093/GJI/GGAA293

407     Martin, E., Castillo, C., Cole, S., Sawasdee, P., Yuan, S., Clapp, R., et al. (2017).

408         Seismic monitoring leveraging existing telecom infrastructure at the SDASA:

409         Active, passive, and ambient-noise analysis. *The Leading Edge*, *36*, 1025–1031.

410         https://doi.org/10.1190/tle36121025.1

411    Nayak, A., & Ajo-Franklin, J. (2021). Measurement of surface-wave phase-velocity

412        dispersion on mixed inertial seismometer – distributed acoustic sensing seismic

413        noise cross-correlations. *Bulletin of the Seismological Society of America*,

414        *111*(6), 3432–3450. https://doi.org/10.1785/0120210028

415    Nayak, A., Ajo-Franklin, J., & Team,   the I. V. D. F. (2021). Distributed Acoustic

416        Sensing Using Dark Fiber for Array Detection of Regional Earthquakes.

417        *Seismological Research Letters*, *92*(4), 2441–2452.

418        https://doi.org/10.1785/0220200416

419    Nishimura, T., Emoto, K., Nakahara, H., Miura, S., Yamamoto, M., Sugimura, S., et

420        al. (2021). Source location of volcanic earthquakes and subsurface

421        characterization using fiber-optic cable and distributed acoustic sensing system.

422        *Scientific Reports*, *11*(1), 1–12. https://doi.org/10.1038/s41598-021-85621-8

423    Piana Agostinetti, N., Villa, A., & Saccorotti, G. (2022). Distributed acoustic sensing

424        as a tool for subsurface mapping and seismic event monitoring: A proof of

425        concept. *Solid Earth*, *13*(2), 449–468. https://doi.org/10.5194/se-13-449-2022

426    Rørstadbotnen, R. A., Eidsvik, J., Bouffaut, L., Landrø, M., Potter, J.,

427        Taweesintananon, K., et al. (2023). Simultaneous tracking of multiple whales

428        using two fiber-optic cables in the Arctic. *Frontiers in Marine Science*,

429        *10*(April), 1–15. https://doi.org/10.3389/fmars.2023.1130898

430    Sladen, A., Rivet, D., Ampuero, J. P., De Barros, L., Hello, Y., Calbris, G., &

431        Lamare, P. (2019). Distributed sensing of earthquakes and ocean-solid Earth

432      interactions on seafloor telecom cables. *Nature Communications*, *10*(1), 1–8.

433      https://doi.org/10.1038/s41467-019-13793-z

434      Walter, F., Gräff, D., Lindner, F., Paitz, P., Köpfli, M., Chmiel, M., & Fichtner, A.

435      (2020). Distributed acoustic sensing of microseismic sources and wave

436      propagation in glaciated terrain. *Nature Communications*, *11*(1).

437      https://doi.org/10.1038/s41467-020-15824-6

438      Wang, H. F., Zeng, X., Miller, D. E., Fratta, D., Feigl, K. L., Thurber, C. H., &

439      Mellors, R. J. (2018). Ground motion response to an ML 4.3 earthquake using

440      co-located distributed acoustic sensing and seismometer arrays. *Geophysical*

441      *Journal International*, *213*(3), 2020–2036. https://doi.org/10.1093/GJI/GGY102

442      Wang, X., Zhan, Z., Williams, E. F., Herráez, M. G., Martins, H. F., & Karrenbach,

443      M. (2021). Ground vibrations recorded by fiber-optic cables reveal traffic

444      response to COVID-19 lockdown measures in Pasadena, California.

445      *Communications Earth & Environment*, *2*(1), 1–9.

446      https://doi.org/10.1038/s43247-021-00234-3

447      Wilcock, W. S. D., & Ocean Observatories Initiative. (2023). Rapid: A Community

448      Test of Distributed Acoustic Sensing on the Ocean Observatories Initiative

449      Regional Cabled Array [Data set]. Ocean Observatories Initiative.

450      https://doi.org/doi.org/10.58046/5J60-FJ89

451    Wilcock, W. S. D., Abadi, S., & Lipovsky, B. P. (2023). Distributed acoustic sensing

452        recordings of low-frequency whale calls and ship noise offshore Central Oregon.

453        *JASA Express Letters*, *3*(2), 026002. https://doi.org/10.1121/10.0017104

454    Williams, E. F., Fernández-Ruiz, M. R., Magalhaes, R., Vanthillo, R., Zhan, Z.,

455        González-Herráez, M., & Martins, H. F. (2019). Distributed sensing of

456        microseisms and teleseisms with submarine dark fibers. *Nature Communications*,

457        *10*(1), 1–11. https://doi.org/10.1038/s41467-019-13262-7

458    Williams, E. F., Zhan, Z., Martins, H. F., Fernández-Ruiz, M. R., Martín-López, S.,

459        González-Herráez, M., & Callies, J. (2022). Surface Gravity Wave

460        Interferometry and Ocean Current Monitoring With Ocean-Bottom DAS.

461        *Journal of Geophysical Research: Oceans*, *127*(5), 1–27.

462        https://doi.org/10.1029/2021JC018375

463    Xiao, H., Gaite, B., & Ruiz-barajas, S. (2022). Locating the precise sources of high-

464        frequency microseisms using distributed acoustic sensing. *Geophysical Research*

465        *Letters*, 0–31. https://doi.org/10.1029/2022GL099292

466    Yang, Y., Zhan, Z., Shen, Z., & Atterholt, J. (2022). Fault Zone Imaging With

467        Distributed Acoustic Sensing: Surface-To-Surface Wave Scattering. *Journal of*

468        *Geophysical Research: Solid Earth*, *127*(6).

469        https://doi.org/10.1029/2022jb024329

470    Yang, Y., Atterholt, J. W., Shen, Z., Muir, J. B., Williams, E. F., & Zhan, Z. (2022).

471        Sub-Kilometer Correlation Between Near-Surface Structure and Ground Motion

472        Measured With Distributed Acoustic Sensing. *Geophysical Research Letters*,

473        *49*(1). https://doi.org/10.1029/2021GL096503

474    Zeng, X., Bao, F., Thurber, C. H., Lin, R., Wang, S., Song, Z., & Han, L. (2022).

475        Turning a Telecom Fiber-Optic Cable into an Ultradense Seismic Array for

476        Rapid Postearthquake Response in an Urban Area. *Seismological Research*

477        *Letters*, *93*(2 A), 853–865. https://doi.org/10.1785/0220210183

478    Zhan, Z. (2019). Distributed acoustic sensing turns fiber-optic cables into sensitive

479        seismic antennas. *Seismological Research Letters*, *91*(1), 1–15.

480        https://doi.org/10.1785/0220190112

481    Zhirnov, A., Stepanov, K., Chernutsky, A., Fedorov, A., Nesterov, E., Svelto, C., et

482        al. (2019). Influence of laser frequency drift in phase-sensitive optical time-

483        domain reflectometry. *Optics and Spectroscopy*, *127*.

484        https://doi.org/10.1134/S0030400X1910031X

485

**Full mailing address for each author**

Minzhe Hu: Laboratory of Seismology and Physics of Earth's Interior, School of Earth and Space Sciences, University of Science and Technology of China, No.96, JinZhai Road Baohe District, Hefei, Anhui, 230026, P.R.China.
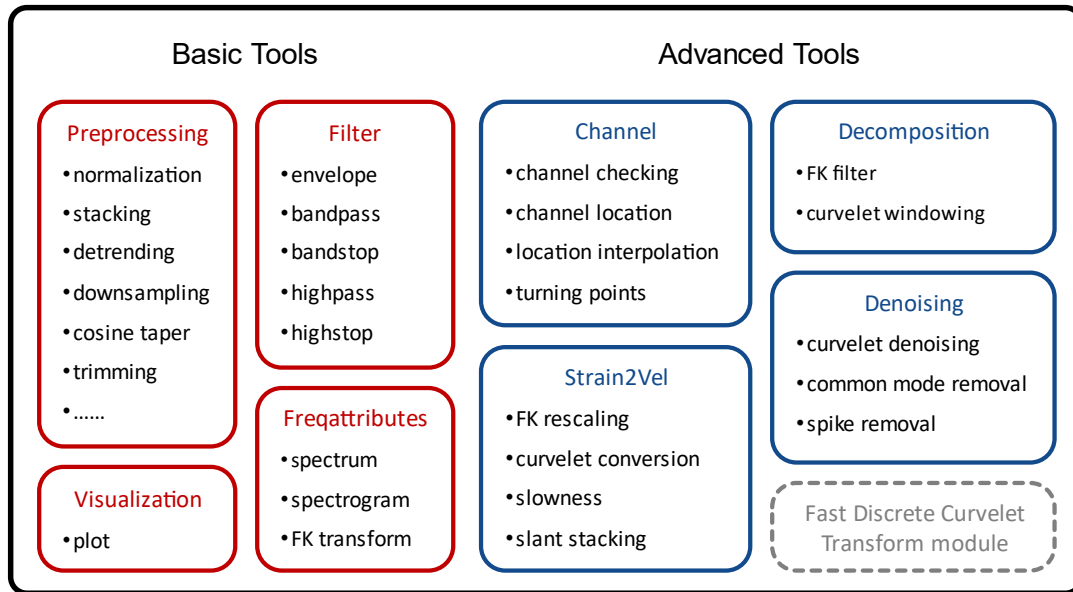
Zefeng Li: Laboratory of Seismology and Physics of Earth's Interior, School of Earth and Space Sciences, University of Science and Technology of China, No.96, JinZhai Road Baohe District, Hefei, Anhui, 230026, P.R.China.

## Basic Tools

**Preprocessing**
- normalization
- stacking
- detrending
- downsampling
- cosine taper
- trimming
- ......

**Filter**
- envelope
- bandpass
- bandstop
- highpass
- highstop

**Visualization**
- plot

**Freqattributes**
- spectrum
- spectrogram
- FK transform

## Advanced Tools

**Channel**
- channel checking
- channel location
- location interpolation
- turning points

**Strain2Vel**
- FK rescaling
- curvelet conversion
- slowness
- slant stacking

**Decomposition**
- FK filter
- curvelet windowing

**Denoising**
- curvelet denoising
- common mode removal
- spike removal

Fast Discrete Curvelet Transform module

494

495 **Figure 1.** Main structure of DASPy toolbox. Each block indicates a module composed

496 of multiple user-facing functions. The modules for basic tools are shown in red boxes,

497 and modules for advanced tools are shown in blue boxes. The module within the gray

498 dotted box is specifically built for discrete fast curvelet transforms.

499
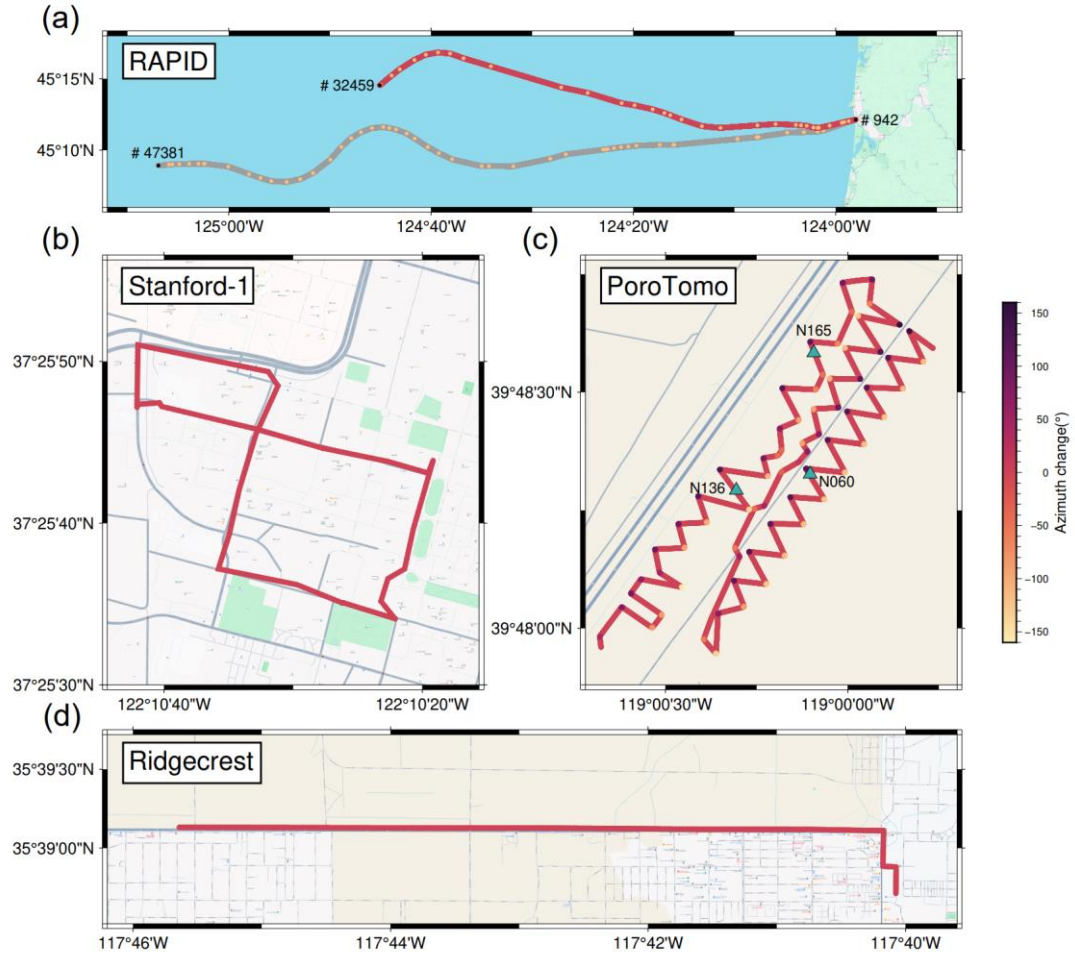
**Figure 2.** Geometry of DAS arrays whose data we used for testing. (a) RAPID DAS

arrays that land at Pacific City, Oregon (Wilcock & Ocean Observatories Initiative.,

2023). The red line indicates the array that we utilized for our test (referring to the north

cable here), which is the same for (b) and (d). The grey line indicates the south cable,

whose data are not used. The black dots represent three points along the cable with

known coordinates and channel numbers, while the orange dots represent the those with

known coordinates but unknown channel number. (b) Stanford campus array in

California (Biondi et al., 2017; Martin et al., 2017). (c) Brady's geothermal field DAS

array (University of Wisconsin, 2016b) and three co-located geophone stations

510    (University of Wisconsin, 2016c) in Nevada. The color of the DAS cable indicates the

511    azimuth change of the cable before and after the corresponding channel. (d) DAS arrays

512    started after the 2019 $M_\mathrm{w}$7.1 Ridgecrest earthquake, California (Atterholt, Zhan, Shen,
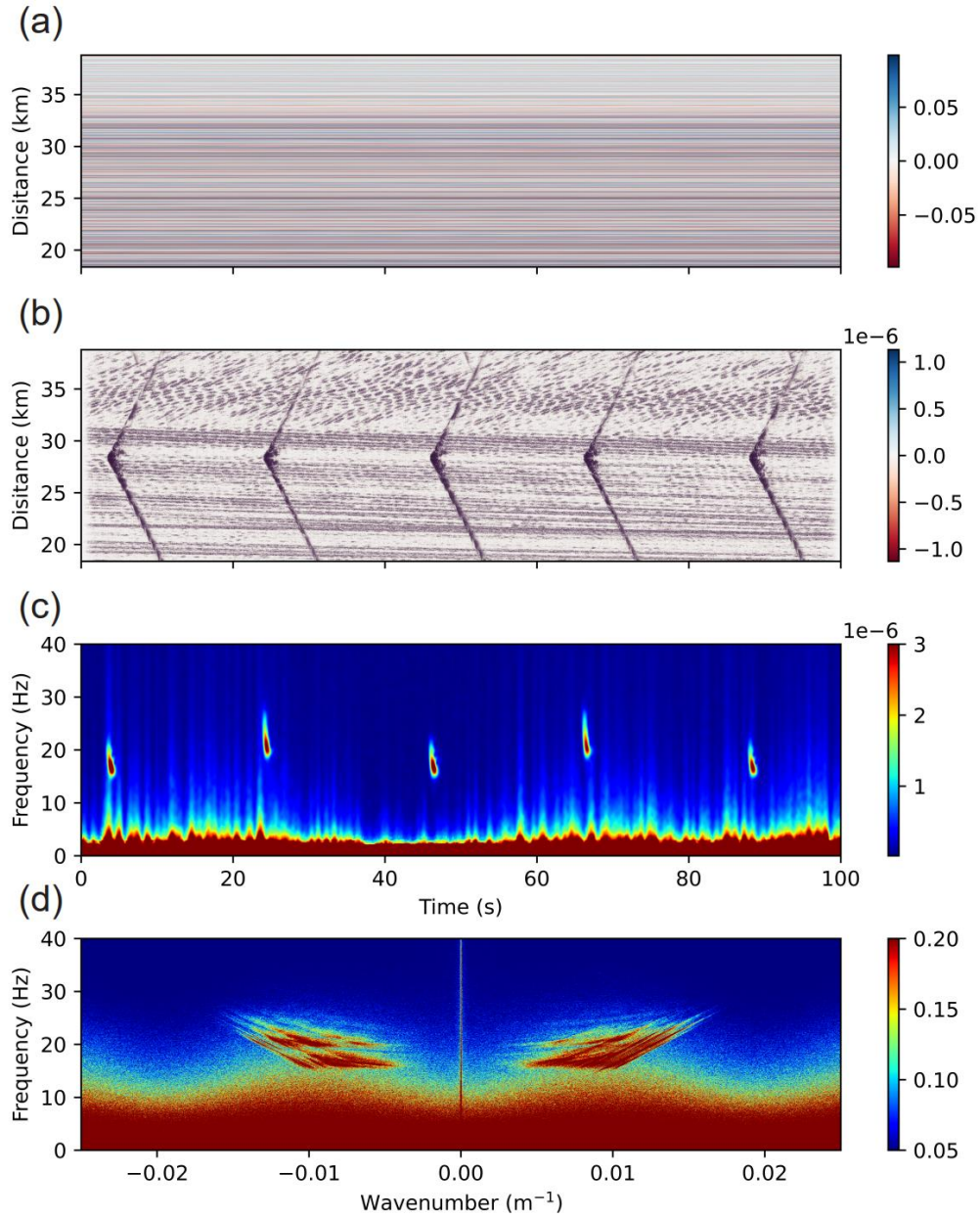
513    et al., 2022; Z. Li et al., 2021).

514

**Figure 3.** Demonstration of signal processing and visualization. (a) Original strain recording for 100 seconds beginning on November 4, 2021, 01:59:02 UT, recorded by the Optasense interrogator on north ocean-bottom cable from RAPID dataset (Wilcock & Ocean Observatories Initiative., 2023). (b) Filter to 15-27 Hz, following Wilcock et al. (2023). (c) Spectrogram averaged over 100 channels. (d) FK spectrum calculated from 2D fast Fourier transform.
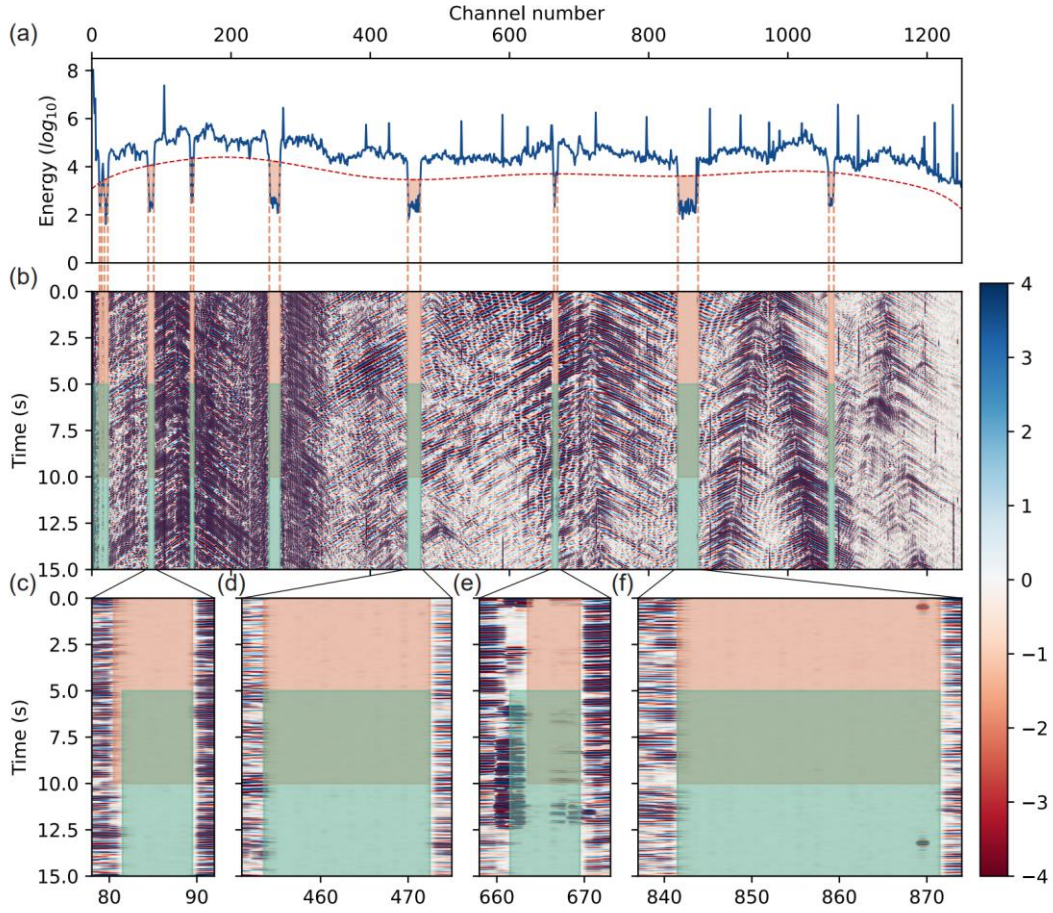
**Figure 4.** Bad channel detection of the DAS array near Ridgecrest, CA. (a) Energy curve (blue line) and thresholds (red dotted line) for bad channel detection. (b) DAS recording of 15-second traffic noise (Atterholt, 2021) used for bad channel detection. Orange areas indicate bad channels detected by our function, while green areas are bad channels picked by Atterholt, Zhan, Shen, et al. (2022). (c)-(f) Zoom-in plot of four parts of the DAS recording. Channel 81 (c) and channels 662&663 (e) are identified differently by our function and Atterholt, Zhan, Shen, et al. (2022).
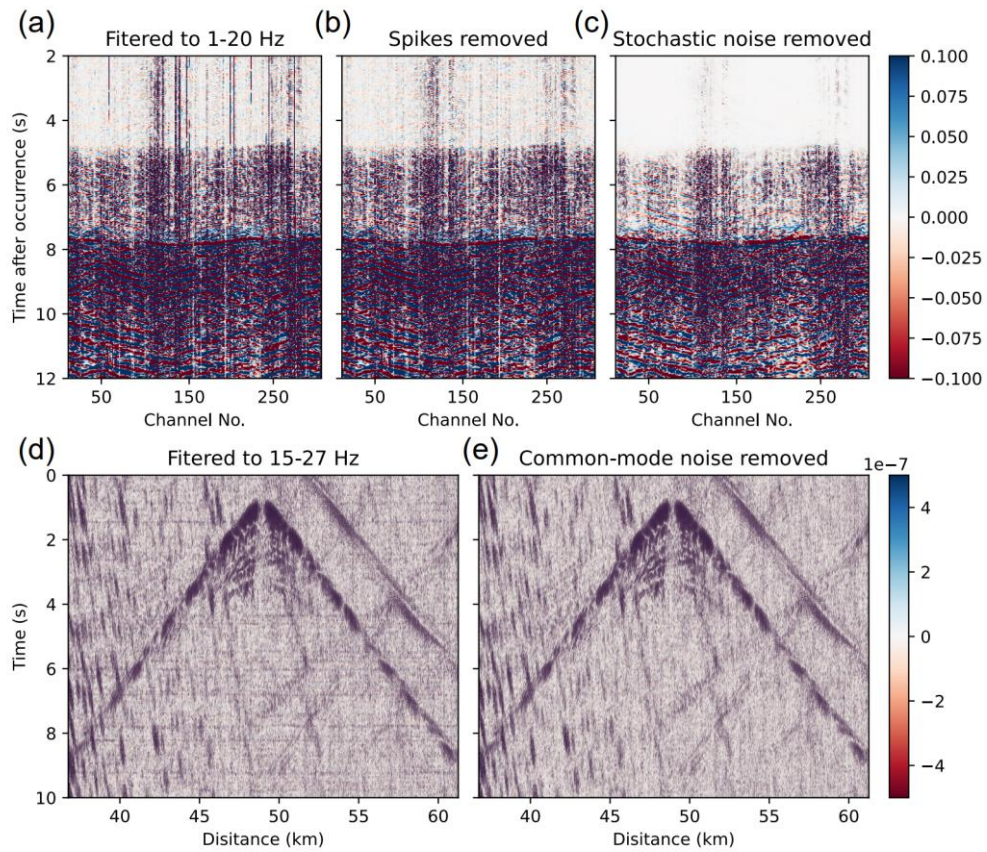
**Figure 5.** Cases of wavefield denoising. (a) Waveforms of an $M_D$ 2.8 earthquake (https://earthquake.usgs.gov/earthquakes/eventpage/nc73940346/executive) recorded by Stanford-1 DAS array (Biondi et al., 2017; Martin et al., 2017). Bad channels are removed and bandpass filter to 1-20 Hz. (b) Waveforms with spikes removed based on (a). (c) Waveforms with stochastic noise removed by curvelet transform based on (b). (d) Strain recording filtered to 15 to 27 Hz for 10 seconds beginning on November 4, 2021, 01:59:22 UT, recorded by the Optasense interrogator on north ocean-bottom cable from RAPID dataset (Wilcock & Ocean Observatories Initiative., 2023). (e) Waveforms with common-mode noise removed based on (d).
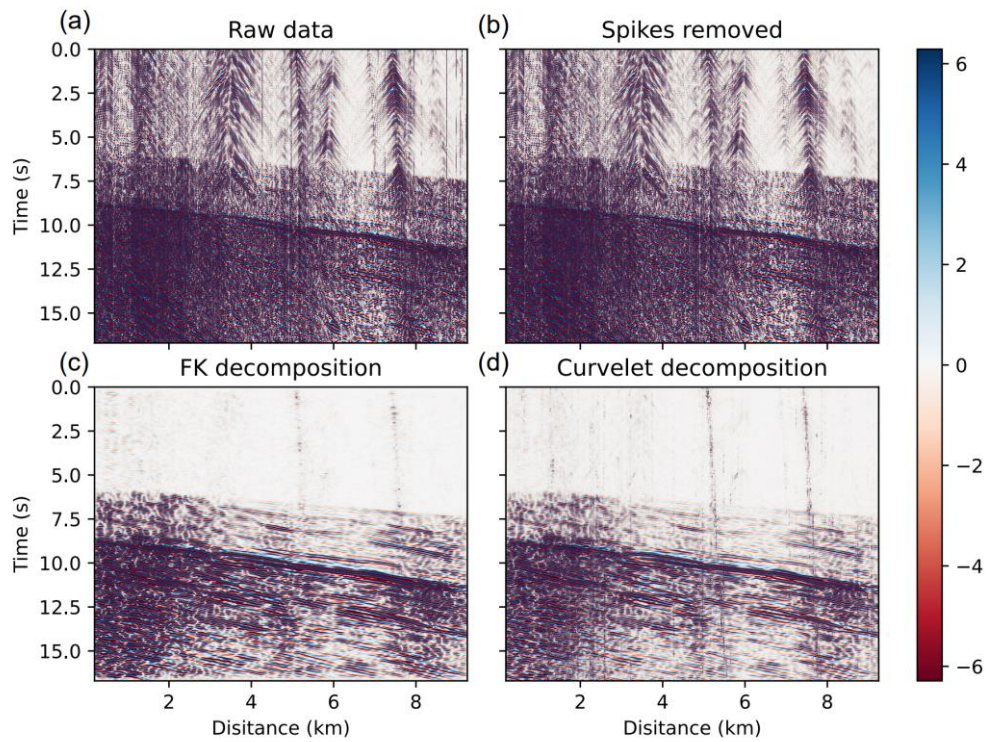
**Figure 6.** An example of wavefield decomposition. (a) Waveforms of an $M_L$ 2.6

earthquake (https://earthquake.usgs.gov/earthquakes/eventpage/ci38972328/executive)

recorded by Ridgecrest DAS array (Z. Li et al., 2021). (b) Waveforms with spikes

removed based on (a). (c) Waveforms with an FK filter to remove energy with an

apparent velocity <1.4 km/s (cosine taper from 1.2–1.6 km/s) based on (b). (d)

Waveforms with curvelet transform and inverse curvelet transform to remove energy
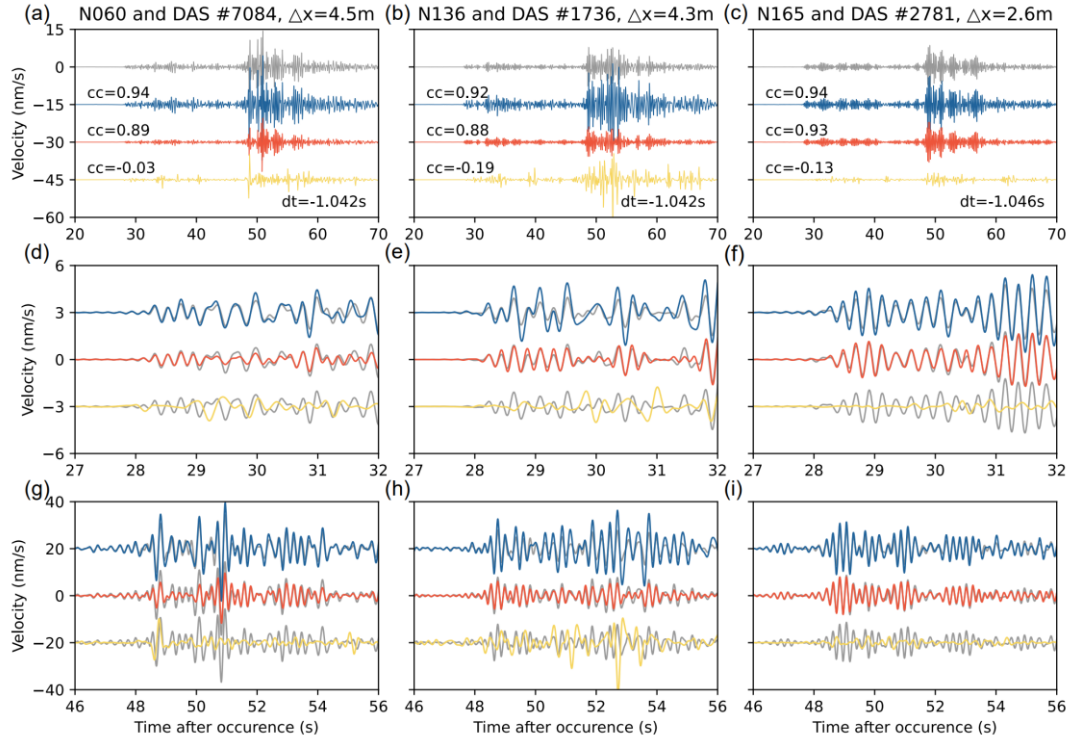
with an apparent velocity <1.4 km/s based on (b).

**Figure 7.** Conversion from strain to velocity by three methods of $M_L$ 4.3 Hawthorne

earthquake (https://earthquake.usgs.gov/earthquakes/eventpage/nn00536374) recorded

by Brady's geothermal field DAS array. (a)-(c) Rotated geophone velocity (grey), and

velocity converted from integrated DAS strain by FK-rescaling (blue), curvelet

transform (red) and time-domain slowness determination (yellow), same as below. All

waveforms are bandpass filtered to 1-5 Hz. (d)-(f) Zoom-in window for P arrival of (a)-

(c). (g)-(i) Zoom-in window for S arrival of (a)-(c).